On the Effects of Tip Clearance and Operating Condition on the Flow Structures Within an Axial Turbomachine Rotor Passage

Yuanchao Li
Department of Mechanical Engineering,
Johns Hopkins University,
Baltimore, MD 21218
e-mail: yli131@jhu.edu

Huang Chen
Department of Mechanical Engineering,
Johns Hopkins University,
Baltimore, MD 21218
e-mail: hchen98@jhu.edu

David Tan
Department of Mechanical Engineering,
Johns Hopkins University,
Baltimore, MD 21218
e-mail: dyt@alum.mit.edu

Joseph Katz[1]
Department of Mechanical Engineering,
Johns Hopkins University,
Baltimore, MD 21218
e-mail: katz@jhu.edu

Effects of tip clearance size and flowrate on the flow around the tip of an axial turbomachine rotor are studied experimentally. Visualizations and stereo-particle image velocimetry (PIV) measurements in a refractive index-matched facility compare the performance, leakage velocity, and the trajectory, growth rate, and strength of the tip leakage vortex (TLV) for gaps of 0.49% and 2.3% of the blade chord, and two flowrates. Enlarging the tip clearance delays the TLV breakup in the aft part of the rotor passage at high flowrates but causes earlier breakup under pre-stall conditions. It also reduces the entrainment of endwall boundary layer vorticity from the separation point where the leakage and passage flows meet. Reducing the flowrate or tip gap shifts the location of the TLV detachment from the blade suction side (SS) upstream to points where the leakage velocity is 70–80% of the tip speed. Once detached, the growth rates of the total shed circulation are similar for all cases, i.e., varying the gap or flowrate mostly shifts the detachment point. The TLV migration away from the SS decreases with an increasing gap but not with the flowrate. Two mechanisms dominate this migration: initially, the leakage jet pushes the TLV away from the blade at 50% of the leakage velocity. Further downstream, the TLV is driven by its image on the other side of the endwall. Differences in migration rate are caused by the smaller distance between the TLV and its image for the narrow gap, and the increase in initial TLV strength with decreasing flowrate and gap.
[DOI: 10.1115/1.4044496]

Keywords: tip gap, tip leakage vortex, axial turbomachine, operating condition, particle image velocimetry

Introduction

The pressure difference between the pressure side (PS) and suction side (SS) of blades in axial turbomachines induces a leakage flow through the tip clearance, which rolls up into the tip leakage vortex (TLV). It is well recognized that these phenomena cause several adverse effects, such as blockage of a part of the flow passage, performance loss, reduction in efficiency, vibrations, rotating instabilities, and stall [1–4]. In spite of efforts to mitigate these effects, they remain a major concern for modern machines, especially for those with a large clearance to blade span ratio. Consequently, considerable effort has been invested to study the effects of tip gap sizes on the performance and flow within axial turbomachines. In recent years, computational studies based on either Reynolds-averaged Navier-Stokes (RANS) solvers (e.g., Refs. [5,6]) or large-eddy simulations (LES) (e.g., Refs. [7–9]) have become the major source for information about tip leakage flows. In parallel, extensive experimental studies have been performed in both linear cascades (e.g., Refs. [10–14]) and rotating machines (e.g., Refs. [15–18]). Prior findings relevant to the present work could be summarized as follows: first, as the reviews of early studies [19,20] have already concluded, increasing the tip gap degrades the performance of axial turbomachines. Furthermore, the critical flow rates for stall inception increases with the gap size [17]. Some studies (e.g., Ref. [6]) conclude that increasing tip clearance reduces machine efficiency; however, other researchers (e.g., Ref. [21]) report the existence of an optimal tip clearance for maximum efficiency. Second, measurements within both linear cascades [10] and rotating machinery [15,16,18] have shown that enlarging the gap increases the TLV size and alters the static pressure distribution along the blade, shifting the highest loading point downstream and delaying the TLV rollup. Third, recent studies [7,11,12] on a cascade geometry have shown that expanding the tip clearance increases the angle between the TLV trajectory and the blade chord and make it more prone to tip leakage cavitation [7] for hydraulic applications. Wider tip clearance is also observed to cause a larger axial velocity, a smaller absolute tangential velocity, and a thicker endwall casing boundary layer downstream of the rotor [15]. Finally, large tip gaps have been shown to increase the flow blockage, which pushes the tip leakage flow further upstream and aligns the TLV with the leading edge (LE) plane [22], a process that presumably enhances the likelihood of rotating instabilities. In the aforementioned cascade, the behavior of TLV under inflow disturbances shows significant fluctuations, which increases with tip gap, and the mechanisms of such unsteadiness differ for small and large clearances [13]. In multi-stage RANS simulations [6] with two tip clearances in the last stage, the interactions between upstream wakes and the tip leakage flow increases with decreasing flow rate and increasing clearance, which contributes to the rotating instability for wide tip gaps.

In early experiments, the characteristic flow structure is usually inferred from measurements in the wake behind the rotor or on the blade surface (e.g., Refs. [11,12,15]). In recent years, particle image velocimetry (PIV) has turned out to be a successful means to study the flow structure inside the passage (e.g., Refs. [23–25]). However, limited optical access to the flow in the rotor passage remains to be a primary reason for the limited amount

[1]Corresponding author.

Contributed by the International Gas Turbine Institute (IGTI) of ASME for publication in the Journal of Turbomachinery. Manuscript received September 11, 2018; final manuscript received July 23, 2019; published online September 10, 2019. Assoc. Editor: Seung Jin Song.

and/or resolution of experimental data available for tip clearance flows. A unique refractive index-matched facility at Johns Hopkins University (JHU) has been assembled to solve this problem. Using transparent blades and casing as well as fluid with the same refractive index facilitates application of multiple optical techniques, including planer and stereo PIV, to study tip leakage flows in waterjet pumps [26–29] as well as blade row interactions in other axial pumps (e.g., Refs. [30–32]). The data presented in this paper has been obtained in an axial compressor-like setting, whose geometry is derived from the first one and half stages of the low-speed axial compressor (LSAC) at NASA Glenn Research Center [33,34]. The rationale for the blade configuration in the JHU facility is s discussed in Refs. [8,9,35]. Some preliminary results focusing on instantaneous flow structures for narrow and wide tip gaps have been published in Refs. [35–38]. The instantaneous velocity and vorticity distributions in the tip region, which are beyond the scope of the present paper, show that: (i) the TLV actually consists of multiple interlacing vortices; (ii) a shear layer containing a series of vortices connects the blade SS tip corner with the TLV; (iii) endwall boundary layer separation occurs at the point where the backward leakage flow meets the main passage flow feeding counter-rotating vortices; and (iv) in the aft part of blade passage, the initially clustered vortex filaments comprising the TLV spread rapidly over a broad area in a process that appears like vortex breakdown reported in prior numerical simulations (e.g., Refs. [39–41]) and experiments [38]. Expanding on the preliminary results [42,43], this paper examines the effects of tip gap size and flow rate on the evolution of the ensemble-averaged flow structures by comparing results obtained for two operating conditions using two sets of blades with nearly the same shape but very different tip gaps. The first gap is quite narrow (<0.5% of the blade chord length), and the second is substantially larger (2.5% of the chord length), exceeding the range of typical axial compressors. As demonstrated, increasing the tip gap or the flow rate change the size, shape, strength, and evolution of the TLV in the rotor passage but not always as expected. The mechanisms affecting the TLV trajectory in the rotor passage are quantified and elucidated.

Experimental Setup and Machine Performance

All the experiments have been performed in the JHU closed-loop test facility. Sketches and detailed descriptions of this system have been provided in multiple previous publications [35,36] and are not included here. Undistorted optical access is achieved by matching the refractive index (1.49) of the transparent acrylic casing and blades with that of the liquid, a 62%–63% by weight aqueous solution of sodium iodide (NaI) [30,44]. This liquid has a specific gravity of 1.84 and a kinematic viscosity of 1.1×10^{-6} m^2/s. As illustrated in Fig. 1, the compressor has three blade rows, consisting of 20 inlet guide vanes (IGV), a 15-blade rotor and a 20-blade stator. As described in Refs. [8,9,36], the blade profiles, and the chord-length-based Reynolds number are matched with those of the first one and a half stages of the LSAC at NASA Glenn. However, the blade aspect ratio at JHU is lower in order to maintain a minimum blade thickness required for operating a machine with acrylic blades in a liquid environment. Furthermore, the number of blades has been reduced to maintain a similar solidity. The Mach number in both facilities is very low; hence, the trends discussed in this study do not account for compressibility effects. A long conical channel with constant through-flow area upstream of the test section is designed to achieve a fully developed turbulent channel flow at the inlet to the IGV. Some relevant geometric parameters of the test section are provided in Table 1. Data presented in this paper are obtained using two sets of rotor blades with nearly the same profile (except for machining errors) but significantly different tip clearance (h). The first has a tip gap of 0.5 mm (0.49% of the chord length or 1.11% of the span), referred as the "narrow gap" in this paper, and the second has a tip gap of

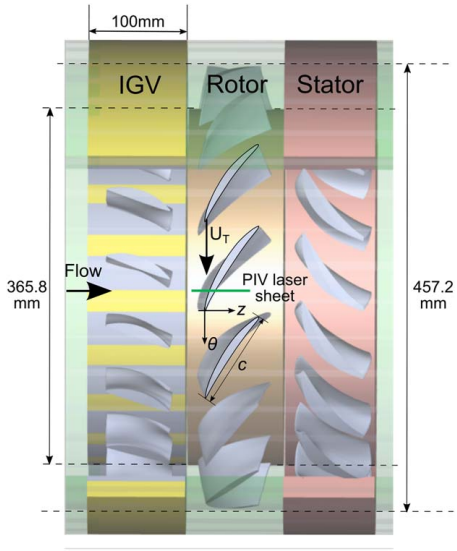

Fig. 1 The test section. All the measurements are performed in the rotor passage.

2.4 mm (2.3% of the chord length and 5.4% of the span), which is referred as the "wide gap." The latter is larger than typical tip clearances in axial compressors. Both tip gap sizes are based on directly measured values. The performance of these machines is characterized by the static-to-static pressure coefficient

$$\psi_{SS} = \frac{P_{exit} - P_{in}}{0.5\rho U_T^2} \tag{1}$$

and the flow rate coefficient

$$\varphi = \frac{V_z}{U_T} \tag{2}$$

Here, ρ is the liquid density, $U_T = 11.47$ m/s is the rotor tip speed at 480 rpm, and $(P_{exit} - P_{in})$ is the static pressure rise across the machine measured using pressure ports located upstream of the IGVs and downstream of the stator. The volumetric flow rate divided by the annular through-flow area in the test section, V_z, i.e., the spatially averaged inflow velocity, is measured by translating a Pitot tube across the pipe in the return line and integrating the velocity profile. As is evident from the results provided in Fig. 2, increasing the tip gap reduces the static-to-static pressure coefficient significantly for the entire range of flow rates, consistent with multiple previous studies (e.g., Refs. [17,19,20]). Detailed measurements are performed at two selected operating conditions, with $\varphi = 0.35$ representing a relatively high flow rate and $\varphi = 0.25$ characterizing a pre-stall condition [36].

Table 1 Relevant parameters of the test section and blade geometries

Casing diameter (D) (mm)	457.20
Hub diameter (d) (mm)	365.76
Rotor diameter (D_R) (mm)	455.92
Rotor blade chord (c) (mm)	102.60
Rotor blade span (mm)	45.08, 43.92
Rotor blade stagger angle (γ) (deg)	58.6
Rotor blade axial chord (c_A) (mm)	53.46
Nominal tip clearance (mm)	0.64 (0.62% of c), 1.8 (1.75%)
Measured tip clearance (h) (mm)	0.5 (0.49% of c), 2.4 (2.3%)
Shaft speed (Ω) (rad s^{-1}) (rpm)	50.27 {480}
Rotor blade tip speed (U_T) (m s^{-1})	11.47
Reynolds number ($U_T c/\nu$)	1.07×10^6

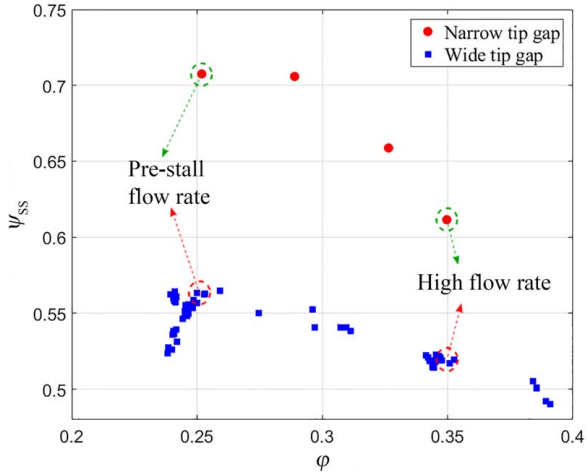

Fig. 2 Performance curves at 480 rpm for the two tip gaps. The two conditions of the present velocity measurements are encircled.

The evolution of the TLV is visualized qualitatively by recording high-speed images of cavitation after reducing the mean pressure over the entire facility. Images are recorded at 2400 frames per second using a PCO®.dimax CMOS camera, with continuous illumination. After increasing the ambient pressure and suppressing any cavitation, quantitative velocity measurements are performed in a series of meridional planes that follow the TLV trajectories using stereo-PIV (SPIV). Details of the optical setups as well as the specifications of seeding particles have been discussed in multiple previous publications [37,38,42,43] and only discussed briefly here. As illustrated in Fig. 3, the sample area is illuminated by a 1 mm thick pulsed laser sheet, and the images of the 13 μm sliver-coated hollow glass particles are recorded by a pair of PCO. 2000, 2048 × 2048 pixels, interline transfer cameras. The 105 mm macro-lenses are inclined to the cameras by the Scheimpflug angles. The time delay between exposures is 20 μs, and the image acquisition times are synchronized with the rotor orientation using a shaft encoder connected to the controller triggering both the laser and the cameras. The calibration of the SPIV system based on the two-step procedure of Wieneke [45], and the image enhancement procedures are discussed in Refs. [36,43]. The commercial software LAVISION DAVIS® is used for performing multi-pass

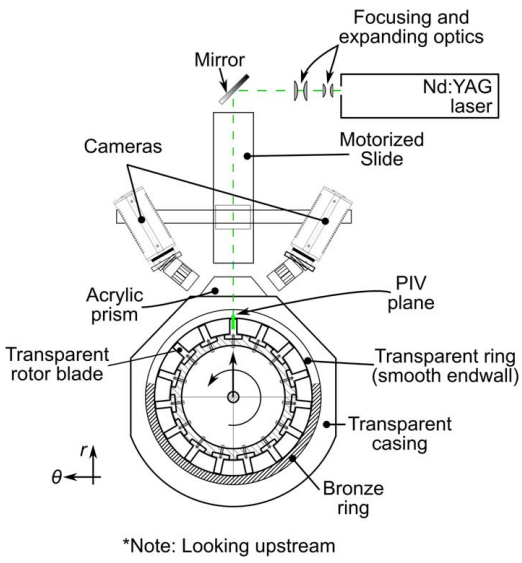

Fig. 3 The SPIV experimental setup

cross-correlations with a final interrogation window of 32 × 32 pixels with 50% overlap to determine the three velocity components. The fields of view are 22.6 × 33.5 mm^2 for $h/c = 0.49\%$ and 23.1 × 31.7 mm^2 for $h/c = 2.3\%$, and the corresponding vector spacings are 0.165 mm and 0.171 mm. Based on convergence tests of the ensemble-averaged quantities and turbulence variables performed using samples of the present data, for each sample plane and condition, 2500 instantaneous realizations are recorded and processed. As discussed in Refs. [27,29,30,46], a typical uncertainty in the instantaneous velocity is about 2% for current settings, taking into account, the number of particles per interrogation window (at least 5), and the displacement between exposures. Ensemble averaging reduces the uncertainty in the average velocity by $\sqrt{2500}$ of the instantaneous value, i.e., to about 0.1%. The corresponding uncertainty in average vorticity is about 1%. Being an integrated quantity, the uncertainty in circulation is of the same order as the velocity. Other potential sources of error include optical distortion, non-uniform particle distributions, insufficient resolution in regions of high-velocity gradients, and slip caused by the difference between the specific gravity of the seed particles (1.6) and that of the fluid. They are minimized using multi-step coarse and fine self-calibration, assuring that each window contains at least five particles, multi-pass correlations, elimination of spurious vectors based on nearby data, use of deformable windows in high shear regions, etc. The estimated effect of these contributors is less than 0.2% [30,47] in instantaneous velocity, much less than other effects.

Results

For each of the two operating conditions and two tip gap sizes, the complete raw dataset consists of a series of high-speed cavitation movies as well as instantaneous and ensemble-averaged distributions of velocity and vorticity. They are used for investigating the effects of tip clearance and flow rate on the distributions of tip leakage flow as well as the strength (circulation), migration, and behavior of the TLV. All the data are presented in a cylindrical coordinate system (z, r, θ), with its origin coinciding with the center of the shaft, and with $z = 0$ and $\theta = 0$ aligned with the rotor tip LE. Flow structure profiles are often presented using a normalized radial coordinate $r^* = 2(r - 0.5d)/(D - d)$, i.e., $r^* = 0$ is located at the hub and $r^* = 1$ at the endwall casing. Definitions of each variable are provided in the nomenclature. The locations of PIV sample planes are identified by s/c, where s is a linear chordwise coordinate indicating the intersection of the (meridional) laser sheet with the blade tip chord, and $s/c = 0$ is located at the tip LE.

Figure 4 shows sample visualization snapshots comparing the TLV location and trajectory for the present four cases. All the images are recorded at the same inlet pressure, but there are noticeable differences in magnification aimed at including the entire cavitating structure within the field of view. All the visualizations are performed with cavitation confined mostly to the tip region. There is a large body of literature on the effect of cavitation on the performance of axial turbomachines, including tests of waterjet pumps performed in the present facility [48,49]. They show that for cavitation to adversely affect the overall machine performance, almost the entire suction side of the rotor blades has to be covered by attached cavitation [50]. For a less developed extent of cavitation, such as the present conditions, it has a negligible effect on the overall machine performance. However, the cavitation is expected to affect the local flow structure, e.g., distributions of vorticity and turbulence in the TLV. Yet, a direct comparison between the TLV trajectory depicted by the cavitation and that derived from the velocity distribution, which is presented later in this paper, show that they are quite consistent. As shown in previous publications (e.g., Refs. [36,42]), tip leakage cavitation occurring in the tip gap is a qualitative indicator for regions with fast tip leakage flow. Figure 4 demonstrates that for each gap, decreasing the flow rate shifts the chord fraction with tip leakage cavitation closer to the blade LE, indicating an upstream migration of the region with

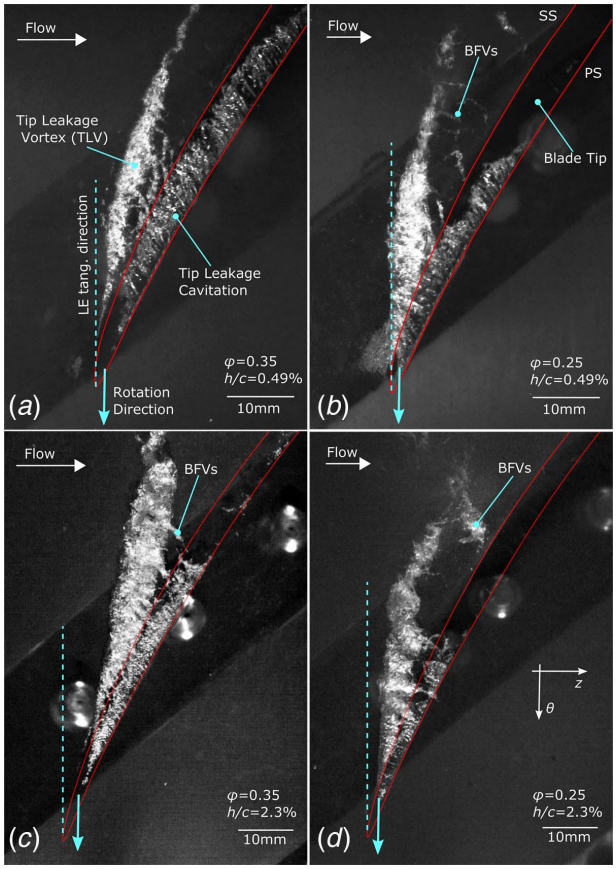

Fig. 4 Sample visualizations of vortical structures near the tip region using cavitation at low pressures. Top row (*a*, *b*): $h/c = 0.49\%$ and bottom row (*c*, *d*): $h/c = 2.3\%$. Left column (*a*, *c*): $\varphi = 0.35$ and right column (*b*, *d*): $\varphi = 0.25$. The dashed lines indicate the circumferential direction at the leading edge, and the solid lines show the blade tip profiles. Note the different magnifications.

primary blade loading, in agreement with LES of the narrow gap flows [9]. For the same flowrate, decreasing the tip gap expands the area with tip leakage cavitation. In all cases, the TLV rolls up, detaches from the blade SS, extends into the passage, and for a while, appears to remain stable. Comparisons to the PIV data provided later shows that in this region, the TLV trajectory inferred from the cavitation images and the velocity distributions is consistent. For both gaps, reducing the flow rate causes earlier TLV rollup, and an increase in the inclination angles with the blade chord. For each flowrate, enlarging the tip gap shifts the location of initial TLV rollup downstream. The latter trend is consistent with previously reported observations on cavitation in axial pumps [51].

In the aft part of the passage, as the TLV starts interacting with secondary cavitating vortices extending from the SS, it narrows down, fluctuates/meanders, and becomes fragmented. In several of our recent papers [9,28,29,35,36], this process has been attributed to TLV breakdown influenced by adverse pressure gradients in the aft part of the passage, seen in other studies as well [39,41]. This phenomenon is characterized by the rapid expansion of the area occupied by vortex filaments associated with the TLV and the disappearance of the distinct TLV center. However, as shown in Ref. [38], the disappearance of the distinct TLV core co-occurs with the formation of "backflow vortices" (BFVs) in the middle of the passage, which extends from the blade SS diagonally upstream. The name is adapted from a related phenomenon occurring in cavitating inducers [52–55]. Figure 4 shows that BFVs form in all cases at the mid-chord. At $\varphi = 0.35$, the stable part of the TLV cavitation is longer for the wide gap, and the BFVs are confined to the space between the TLV and the blade SS. At $\varphi = 0.25$, the number and size of BFVs increase in the region of TLV breakdown (Figs. 4(*b*) and 4(*d*)), suggesting, as proposed in Ref. [38], that they play a significant role in the TLV fragmentation. However, in identifying the causes of TLV fragmentation, we cannot decouple the effects of adverse pressure gradients in the aft part of the passage and flow induced by the BFVs. Hence, this paper still refers to the fragmentation of the TLV as breakup although it might not necessarily correspond to the classical vortex breakup. It should also be noted that TLV breakdown has been observed in all the axial turbomachines that we have tested to-date, including two waterjet pumps at varying operating conditions [9,28,29,35,36], indicating that it is not unique to the present setup. Furthermore, under pre-stall conditions, the BFVs become quite large, intermittently extending from the SS of one blade to the PS of the neighboring blade [38]. When they penetrate to the next passage across the tip gap or reach the next passage around the leading edge of the next blade, they trigger a similar phenomenon in that passage. Intermittent propagation around the leading edge becomes the typical mode during early phases of the stall, suggesting that the BFVs generate spike type stall [56–58].

Samples of characteristic ensemble-averaged velocity distributions (U_z, U_r, U_θ) at $s/c = 0.44$ for both tip gaps and flow rates are provided in Fig. 5. They are aimed at setting the framework for subsequent discussions. Here, in-plane components (U_z/U_T, U_r/U_T) are shown as vectors, and the out-of-plane component, U_θ/U_T, is presented in color contours. The number of vectors is reduced (diluted) in each plot by the indicated ratios for clarity, i.e., the actual data density is higher than that indicated by the vectors. The corresponding distributions of $\langle\omega_\theta\rangle = \partial U_r/\partial z - \partial U_z/\partial r$, where $\langle\rangle$ indicates ensemble averaging, are also plotted as black contour lines (solid for positive values and dashed for negative ones). Several characteristic features are evident: First, in all cases, after passing through the tip clearance, the leakage flow impinges on the main passage flow upstream of the TLV center, generating a "stagnant region" for the in-plane components, and causing endwall boundary layer separation, which feeds negative vorticity into the passage. Second, consistent with prior observations in other axial machines [29], in all cases, U_θ has a positive peak under the TLV center and a minimum diagonally above this center, which at $\varphi = 0.35$ become negative. In a reference frame rotating with the blade, high positive U_θ implies a low velocity relative to the blade. The peak of positive $\langle\omega_\theta\rangle$, i.e., the mean TLV center, is located in a region with high radial gradients of U_θ. As discussed in Ref. [37], which shows the evolution of U_θ for the present gaps, the area of elevated positive U_θ increases with s/c and with decreasing flow rate. Once the vortex breakdown occurs, this high U_θ area grows rapidly and covers a substantial fraction of the tip region [29,36,37,39,41]. Third, near the blade tip, $U_\theta > 0$ for the narrow gap in both flow rates. Conversely, for the wide gap, $U_\theta < 0$ at $\varphi = 0.35$ (Fig. 5(*a*)), indicating a leakage flow moving circumferentially against the direction of blade rotation. In contrast, at $\varphi = 0.25$ (Fig. 5(*c*)), the entire tip clearance is filled with fluid with $U_\theta > 0$, presumably since the leakage flow entrains fragments of the previous TLV. In this plane, the instantaneous realizations (not shown), which cover both sides of the blade, show that the pressure side contains multiple fragments of the previous TLV, after it breaks down [35,38]. Consequently, the corresponding ensemble-averaged circumferential vorticity distribution has a broad area with elevated $\langle\omega_\theta\rangle$ around the PS of the blade (Fig. 6(*f*)). This observation is also consistent with the nearly circumferential TLV trajectory in the cavitation images (Fig. 4(*d*)).

Further insight can be obtained by examining the distributions of three vorticity components for the wide gap. Following procedures discussed in Wu et al. [29], the 3D ensemble-averaged vorticity is obtained by recording SPIV data in a series of 11 closely spaced meridional planes located around $s/c = 0.44$. They extend from $s/c = 0.432$ to 0.442, and the distance between them is $\Delta(s/c) = 0.00092$. These planes are separated by an angular gap of

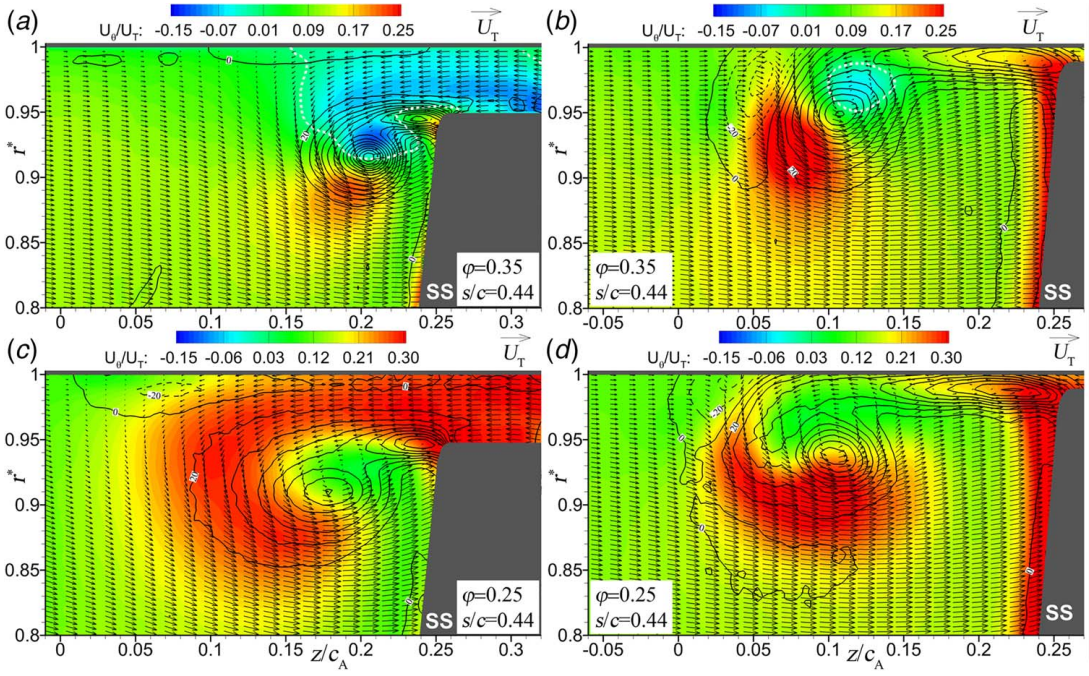

Fig. 5 Samples of ensemble-averaged distributions of circumferential velocity (color contours) and in-plane velocity components (vectors) diluted by 4:1 in the *z*-direction at *s/c* = 0.44. The black contours show the distributions of normalized circumferential vorticity ($\langle\omega_\theta\rangle/\Omega$). The increment between lines is 20. The white dashed lines highlight the location of zero circumferential velocity. Top row (*a*, *b*): $\varphi = 0.35$ and bottom row (*c*, *d*): $\varphi = 0.25$. Left column (*a*, *c*): *h/c* = 2.3% and right column (*b*, *d*): *h/c* = 0.49%.

3.54×10^{-4} rad, corresponding to circumferential distances of 0.081 mm at the endwall casing and 0.073 mm at the bottom of the field of view. Both are much smaller than the in-plane vector spacing. After ensemble averaging of data in each plane, second-order finite differencing is used to calculate the two vorticity components involving out-of-plane velocity gradients, $\langle\omega_z\rangle = \partial U_\theta/\partial r - r^{-1}(\partial U_r/\partial\theta - U_\theta)$ and $\langle\omega_r\rangle = r^{-1}\partial U_z/\partial\theta - \partial U_\theta/\partial z$. The data from all the 11 planes are circumferentially averaged to improve the quality of calculated out-of-plane gradients. The resulting distributions of $\langle\omega_z\rangle$ (Figs. 6(*a*) and 6(*b*)), $\langle\omega_r\rangle$ (Figs. 6(*c*) and 6(*d*)), and $\langle\omega_\theta\rangle$ (Figs. 6(*e*) and 6(*f*)) are provided for $\varphi = 0.35$ (left column) and $\varphi = 0.25$ (right column). To assist in the ensuing discussion, the contours of $\langle\omega_\theta\rangle$ are also marked using black lines. Noting the differences in the color scales, $\langle\omega_\theta\rangle$ is the dominant vorticity component. Although the spatial distributions and magnitudes of vorticity components differ under the two operating conditions, several common features persist. First, for both flow rates, the TLV mean core area, where $\langle\omega_\theta\rangle$ peaks, is associated with elevated negative $\langle\omega_z\rangle$ and positive $\langle\omega_r\rangle$, the origins of which can be seen from the dominant spatial gradients in U_θ evident in Fig. 5. As the vortex increases in size with decreasing flow rate, the magnitudes of all three vorticity components near the TLV center decrease. Second, the expected impact of the boundary layers on the blade, with $\langle\omega_r\rangle > 0$ along the PS and $\langle\omega_r\rangle < 0$ along the SS of the blade, is evident. Third, a region with high $\langle\omega_r\rangle < 0$ region is located above the PS tip corner, in the region where $\partial U_\theta/\partial z > 0$, as the leakage flow enters the tip gap. Fourth, there are broad areas with $\langle\omega_z\rangle > 0$ radially inward from (under) the TLV center, in the region where the magnitude of U_θ gradually decreases. In Ref. [38], it was shown that this vorticity plays an important role in the formation of BFVs and the development of large scale instabilities associated with the onset of stall. Finally, the significant difference appears in the high $\langle\omega_\theta\rangle$ shear layer connecting the blade tip SS with the TLV center. Consistent with the gradients in U_θ, at $\varphi =$ 0.35, most of this shear layer is located in a region with $\langle\omega_z\rangle < 0$, whereas at $\varphi = 0.25$ $\langle\omega_z\rangle > 0$. It should be noted that many of the features depicted in Figs. 4–6, e.g., formation of a shear layer connecting the TLV to the SS corner, endwall boundary layer separation ahead of the TLV, high circumferential velocity below the TLV center, formation of BFVs, and TLV breakdown, have been observed in all the axial turbomachines that we have tested to-date [9,28,29,35,36].

In the following discussion, the distributions of $\langle\omega_\theta\rangle$ are used to examine the tip gap effects on the evolution of flow structure in the tip region for both flow rates. Series of $\langle\omega_\theta\rangle$ plots comparing the evolution of the TLV for $\varphi = 0.35$ and $\varphi = 0.25$ are presented in Figs. 7 and 8, respectively. In each series, the $\langle\omega_\theta\rangle$ plots for the two gaps at the same *s/c* are placed above each other using the same coordinate system. Corresponding plots are also shifted axially, matching their z/c_A locations, in order to highlight differences in the TLV trajectories. The discussion examines the evolution of the TLV center (labeled as A), the shear layer connecting the blade SS tip corner to the TLV (labeled as B), and the layer of negative $\langle\omega_\theta\rangle$ originating from the point of endwall boundary layer separation (labeled as C). Several trends are evident: (i) In both flowrates, the TLV rolls up near the blade SS corner and then migrates away from the blade. Increasing the tip clearance delays the vortex rollup and its detachment from the blade SS, consistent with the cavitation images. As quantified later, this slower migration rate away from the blade is caused in part by a lower TLV strength and in part by its larger distance from the endwall, which reduce the velocity induced by the image vortex across the casing. (ii) At large *s/c*, the previously discussed vortex breakdown occurs, characterized by a rapid increase in the area with elevated $\langle\omega_\theta\rangle$, and a substantial decrease in the magnitude of peak $\langle\omega_\theta\rangle$. Trends with clearance size depend on the flow rate. At $\varphi = 0.25$ (Fig. 8), vortex breakdown occurs earlier for the wide gap, as the $\langle\omega_\theta\rangle$ peak in the TLV center diminishes at $s/c \sim 0.66$. Formation of BFVs and their migration from one passage to the next across the wider tip gap [38] is a major contributor to this early breakup. As the cavitation images show, these vortices are less likely to penetrate across the narrow gap. Being intermittent, the BFVs are evident from the instantaneous distributions of ω_θ, which are not included in this paper but can be seen in Ref. [38]. However, it is

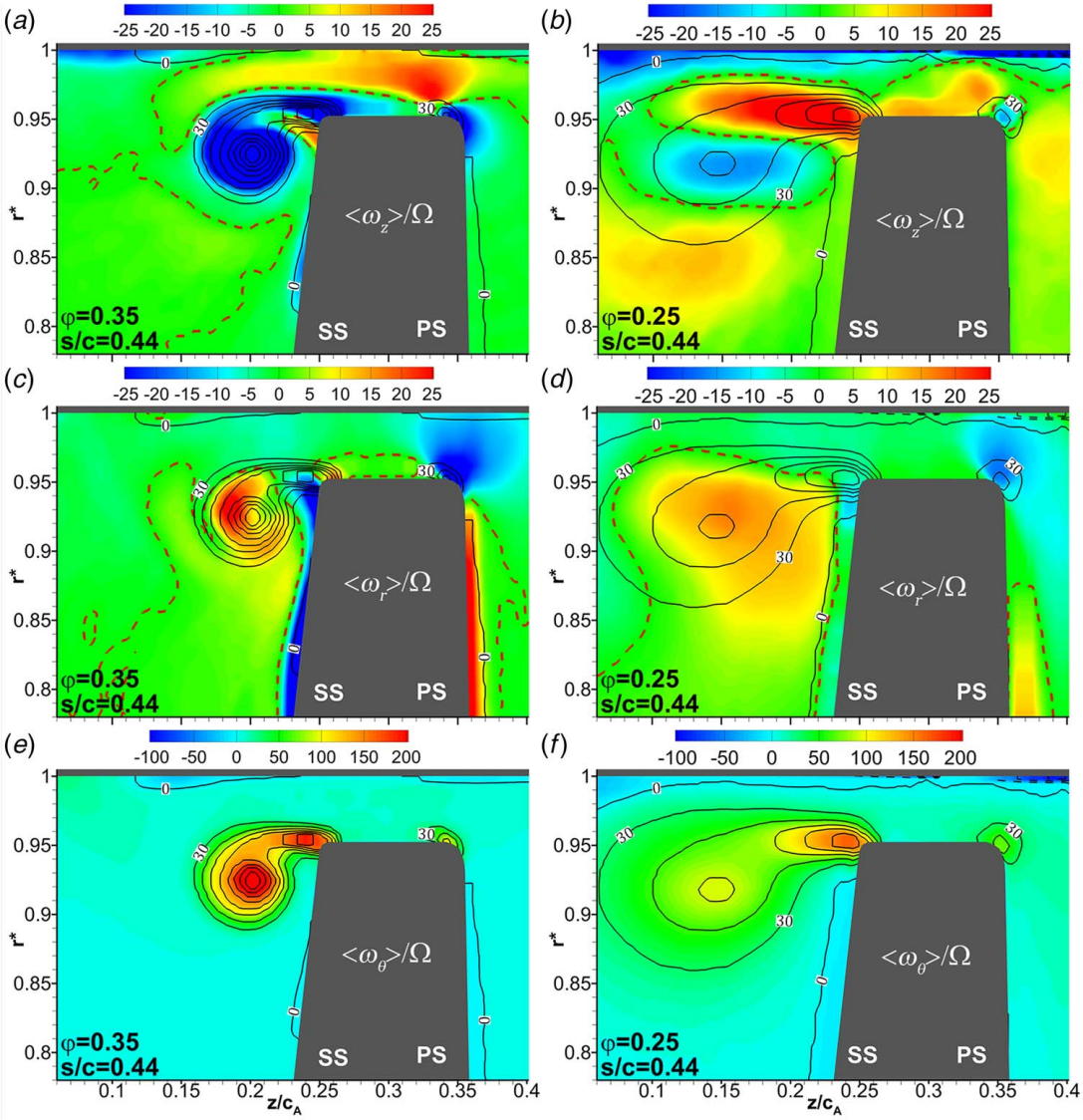

Fig. 6 Distributions of three vorticity components at $s/c = 0.44$ for $\varphi = 0.35$ (left column) and $\varphi = 0.25$ (right column). Color contours of (*a*, *b*) $\langle\omega_z\rangle/\Omega$, (*c*, *d*) $\langle\omega_r\rangle/\Omega$, and (*e*, *f*) $\langle\omega_\theta\rangle/\Omega$ with dashed lines marking zero values are superimposed on black contours of $\langle\omega_\theta\rangle/\Omega$. The increment between black contour lines is 30. Note the differences in scales.

difficult to observe them in the plots of $\langle\omega_\theta\rangle$, which are dominated by the persistent TLV and shear layer, and the impact the BFV is limited to an area with elevated $\langle\omega_\theta\rangle$ radially inward from the TLV. However, as shown in Fig. 6(*b*), the BFVs leave a clear signature in the distributions of $\langle\omega_z\rangle$ centered around $r^* = 0.83$. In contrast, at $\varphi = 0.35$ (Fig. 7), increasing the tip clearance delays the onset of vortex breakdown, as the $\langle\omega_\theta\rangle$ peak in the TLV center remains distinct at $s/c \sim 0.87$ for the wide gap but diminishes earlier for the narrow gap. At this flow rate, the BFVs remain small and confined to the space between the TLV and the blade SS. Hence, they typically do not reach the PS of the next blade and do not penetrate across the gap. (iii) In essentially all cases, the TLV is connected to the SS tip corner by a shear layer (B) with high positive vorticity. It feeds vorticity into the TLV and defines the location of transition from the backward leakage flow to forward passage flow radially inward from it. (iv) Enlarging the tip gap alters the shape and structure of the negative $\langle\omega_\theta\rangle$ layer (C) originating from the point of endwall separation. In both flow rates, for the narrow gap, this layer is entrained radially inward by the TLV, and subsequently surrounds the TLV core, creating a negative vorticity ring around the positive vorticity center. Conversely, for the wide gap, the negative $\langle\omega_\theta\rangle$ layer remains largely above the TLV throughout the passage, although it detaches eventually from the endwall. This diminished entrainment is also likely affected by the larger distance between the TLV and endwall boundary layer, and the differences in the TLV strength during the early phases of vortex rollup.

The evolution of the axial and radial coordinates of the TLV center based on the location of the $\langle\omega_\theta\rangle$ peaks, z_{TLV}/c_A and r^*_{TLV}, respectively, are plotted in Figs. 9(*a*) and 9(*b*). The axial positions of the endwall separation point, z_{sep}/c_A, where U_z changes sign upstream of the TLV near $r^* = 1$, are provided in Fig. 9(*c*). The conditions corresponding to specific symbols, line types, and colors used in these plots are maintained in subsequent figures throughout this paper. For one of these cases, the wide gap at $\varphi = 0.35$, the distributions of z_{TLV} and z_{sep} are superimposed on the ensemble-averaged cavitation images (150 images) for the same condition in Fig. 9(*d*). Starting with the latter, evidently, at low s/c (<0.44), z_{TLV} and the axial extent of the cavitation overlap. At mid-chord ($0.44 < s/c < 0.76$), where the TLV location appears to be stable, z_{TLV} is nearly aligned with the center of the cavitating region. Further downstream, after the vortex breaks down, the average

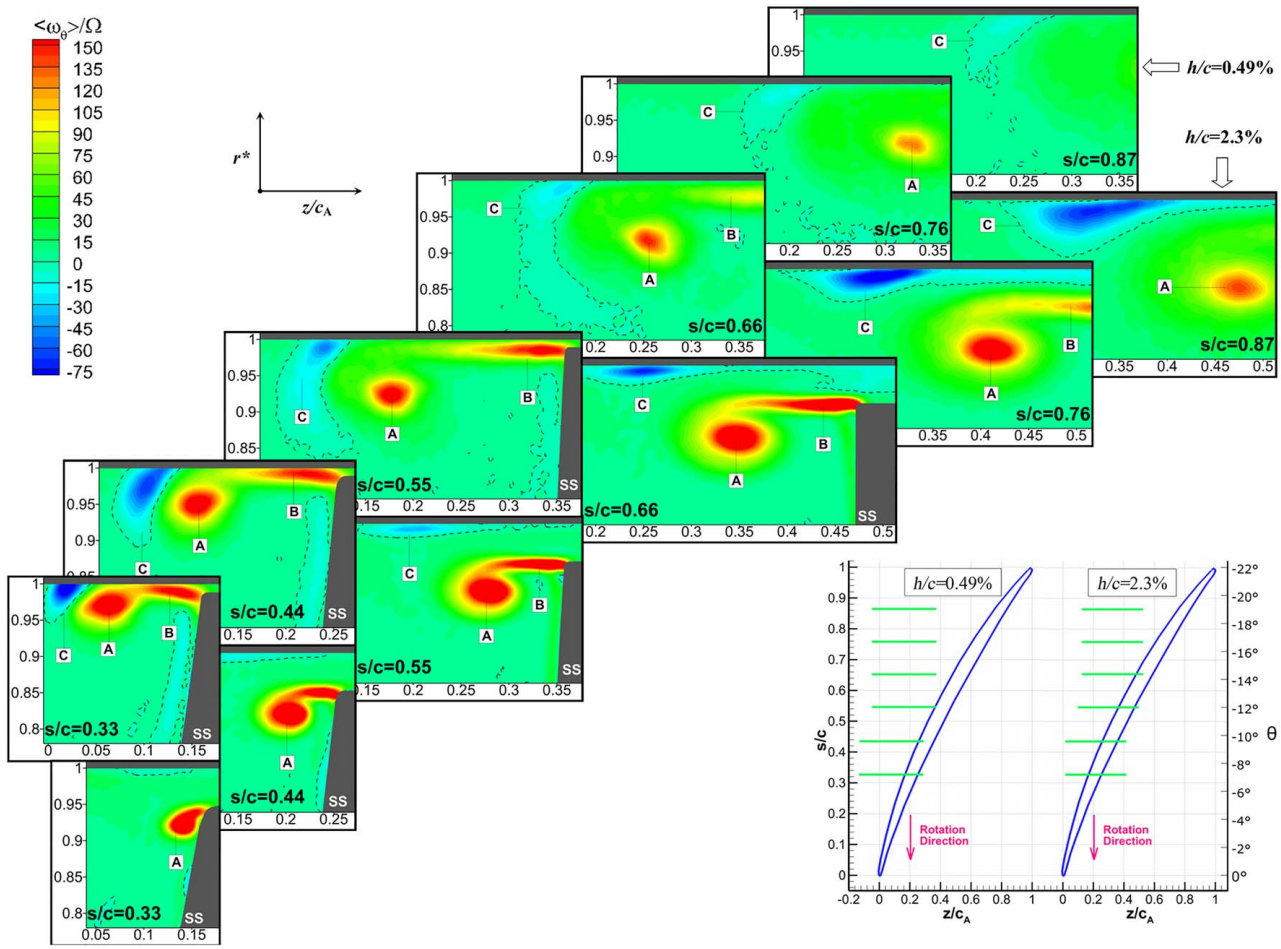

Fig. 7 Contour plots of the distributions of $\langle\omega_\theta\rangle/\Omega$ at $\varphi = 0.35$ for $h/c = 0.49\%$ (top row), and $h/c = 2.3\%$ (bottom row). Dashed lines indicate the location of $\langle\omega_\theta\rangle/\Omega = 0$. Bottom right: Location of the sample planes.

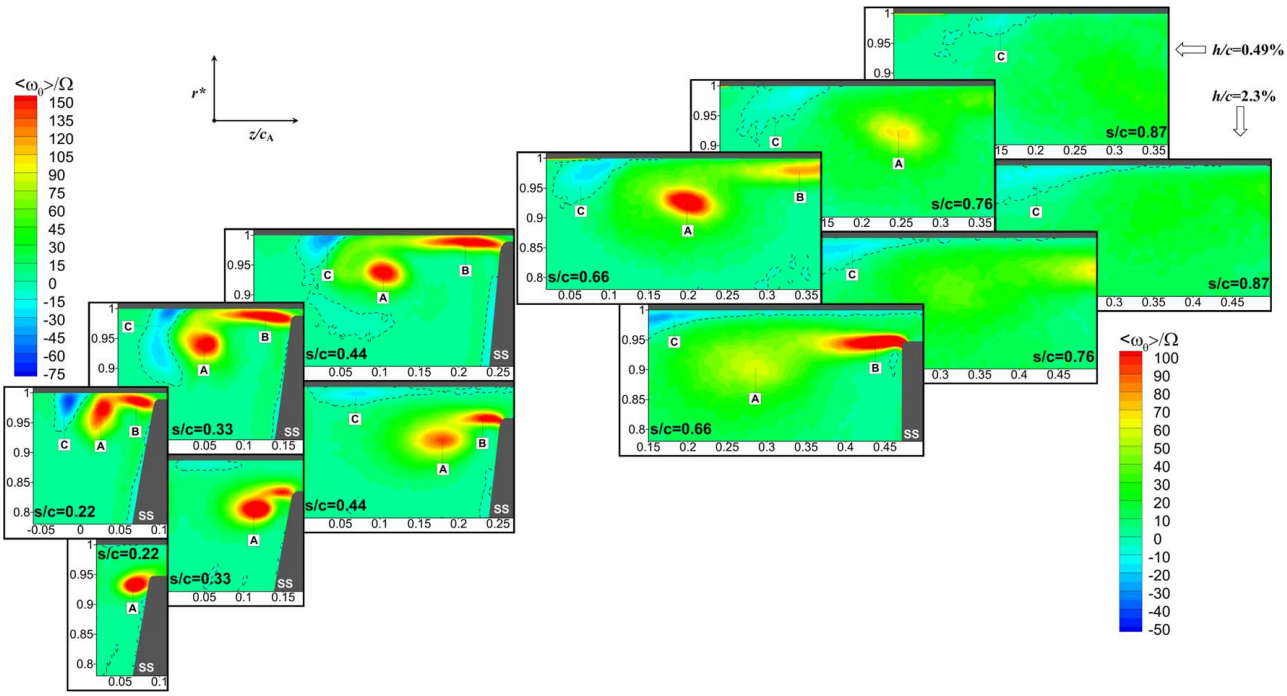

Fig. 8 Contour plots of the distributions of $\langle\omega_\theta\rangle/\Omega$ at $\varphi = 0.25$ for $h/c = 0.49\%$ (top row), and $h/c = 2.3\%$ (bottom row). Dashed lines indicate the location of $\langle\omega_\theta\rangle/\Omega = 0$. Note the difference in color scales.

intensity decreases due to TLV meandering, and its center is no longer aligned with the SPIV-based TLV center. In all cases, the cavitating region is confined between the SS and z_{sep}. This comparison demonstrates that the cavitation does not alter the vortex trajectory prior to breakup significantly. A very similar correlation between the cavitation images and SPIV data has been observed for the other cases (not shown). Therefore, the images can be used for assessing the initial point of TLV rollup, and the vortex trajectory in regions where it is stable. In subsequent discussions about the evolution of TLV, the location of initial TLV rollup is deduced from the averaged cavitation images. These vortex origins are indicated in Fig. 9(*a*).

In all cases, the TLV center gradually migrates away from the blade SS corner, but the rates vary. The axial distance between the TLV and the SS (Fig. 9(*a*)) increases with decreasing tip gap size (for the same flow rate) and with decreasing flow rate (for the same gap). As quantified later, contributors to these trends include the location of vortex rollup, strength, proximity to its image on the other side of the endwall, and breakup. Similar trends are observed for the evolution of z_{sep} in Fig. 9(*c*), but inherently, $z_{TLV} > z_{sep}$. Figure 9(*b*) shows that for all cases, the vortex is already located radially inward from the SS tip corner in the first SPIV sample plane, and r^*_{TLV} for the wide gap is inherently smaller than that of the narrow gap. As the TLVs grow, their centers migrate radially inward, consistent with results of numerical simulations for a compressor cascade reported in Refs. [59]. At low *s/c*, the radial migration rate is faster for the narrow gap (in both flow rates), but further downstream, all the r^*_{TLV} plots seem to have similar slopes. Several factors are likely to affect the radial migration, including (i) the growth and expansion of the vortex with increasing *s/c*, (ii) negative radial velocity induced by the shear layer, (iii) flow induced by the negative vortices originating from the endwall separation point especially for the narrow gap, and (iv) radial pressure gradients near the endwall separation point, which involves an in-plane "stagnation." An interesting implication of the data in Figs 7–9 is that the performance degradation occurring as the tip gap is widened is *not* associated with a drastic increase in the area influenced directly by the TLV, presumably, the TLV-induced blockage. Conversely, Figs. 9(*a*) and 9(*c*) show that increasing the tip gap keeps the TLV closer to the blade SS. Specific reasons for this trend are quantified later. Furthermore, Fig. 9(*b*) shows that in spite of differences in the radial location of the SS corner, i.e., the point of TLV rollup, by mid-chord, the values of r^*_{TLV} for a wide gap and low flow rate are only 2% smaller than those corresponding to the narrow gap, i.e., they are not strikingly different (Fig. 9(*b*)). Finally, Fig. 7 shows for high flow rate that vortex breakdown and the associated expansion of the area occupied by the TLV actually occur earlier for the narrow gap.

Figure 10 provides quantitative assessment for the evolution of TLV structure and strength, including the peak value of $\langle\omega_\theta\rangle$ ($\langle\omega_\theta\rangle_{peak}$) in the TLV center, the total positive circulation (Γ_{tot}) in the area covering both the TLV and the shear layer, the positive circulation within the TLV only (Γ_{TLV}), and the remaining positive circulation in the shear layer ($\Gamma_{SL} = \Gamma_{tot} - \Gamma_{TLV}$). The circulation ($\Gamma = \iint \langle\omega_\theta\rangle dA$) is calculated by spatially integrating $\langle\omega_\theta\rangle$ over areas where $\langle\omega_\theta\rangle$ exceeds threshold levels selected to be 0.1 $\langle\omega_\theta\rangle_{peak}$. The results presented in Figs. 10(*b*)–10(*d*) are restricted to planes where the entire TLV and the shear layer are located within the SPIV sample area. When presented together with trends of the total vortex strength, the variations in $\langle\omega_\theta\rangle_{peak}$ (Fig. 10(*a*)) could be used for characterizing the clustering of vortex filaments at low *s/c* and their fragmentation after the breakup in the aft part of the passage. While the difference between values of $\langle\omega_\theta\rangle_{peak}$ at the two flow rates is small for the narrow gap, they are striking for the wide gap. For the latter, the much higher values of $\langle\omega_\theta\rangle_{peak}$ at mid-chord at high flowrate in spite of having the lower circulation (Fig. 10(*c*)) indicate that the vortex filaments comprising the TLV are tightly clustered. In contrast, the early breakdown along with ingestion of turbulence across the tip gap at low flow rate causes a rapid decrease in peak vorticity in spite of the growth of circulation.

In all cases, as expected, Γ_{tot}, Γ_{TLV}, and Γ_{SL} grow with *s/c*, as vortex filaments are continuously shed from the blade tip. Since the blade loading and location of TLV rollup move closer to the blade LE and the pressure rise increases with decreasing flow rate, the corresponding Γ_{tot} (Fig. 10(*b*)) values are higher. For the same flow rate, increasing the tip gap reduces Γ_{tot}, presumably reflecting the effects of the reduction in performance and downstream shift of blade loading. Accordingly, the differences between gaps decrease but do not vanish with increasing *s/c*. A fraction of Γ_{tot} is entrained into the TLV (Fig. 10(*c*)), and the rest, e.g., more than 40% of Γ_{tot}, for the narrow gap, is distributed along the shear layer (Fig. 10(*d*)). Increasing the tip gap results in a higher slope of Γ_{TLV} versus *s/c* for both flowrates. The earlier rollup and the faster migration rate of the TLV from the SS (Figs. 7 and 8), which leaves larger portions of the circulation in the shear layer, for the narrow gap, are likely contributors to this trend. Accordingly, both the slope and the magnitude of Γ_{SL} increase with decreasing tip gap. For both gaps, Γ_{TLV} and Γ_{SL} persistently

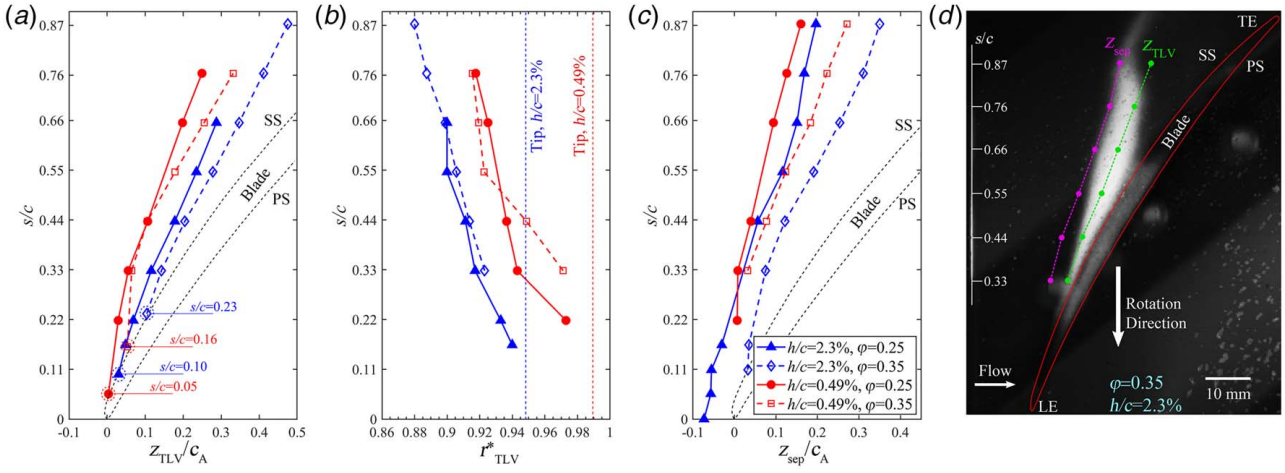

Fig. 9 (*a*) Axial (z_{TLV}/c_A), and (*b*) radial (r^*_{TLV}) locations of the TLV peak circumferential vorticity. (*c*) The axial location of the endwall boundary layer separation point (z_{sep}/c_A), where the leakage flow meets the main passage flow. (*d*) Averaged cavitation image showing the trajectory of TLV with dashed line representing the locations of z_{TLV} and z_{sep} for $h/c = 2.3\%$ and $\varphi = 0.35$. The locations of TLV detachment from the blade, s_{det}, estimated from the cavitation images are labeled as dashed circles in (*a*).

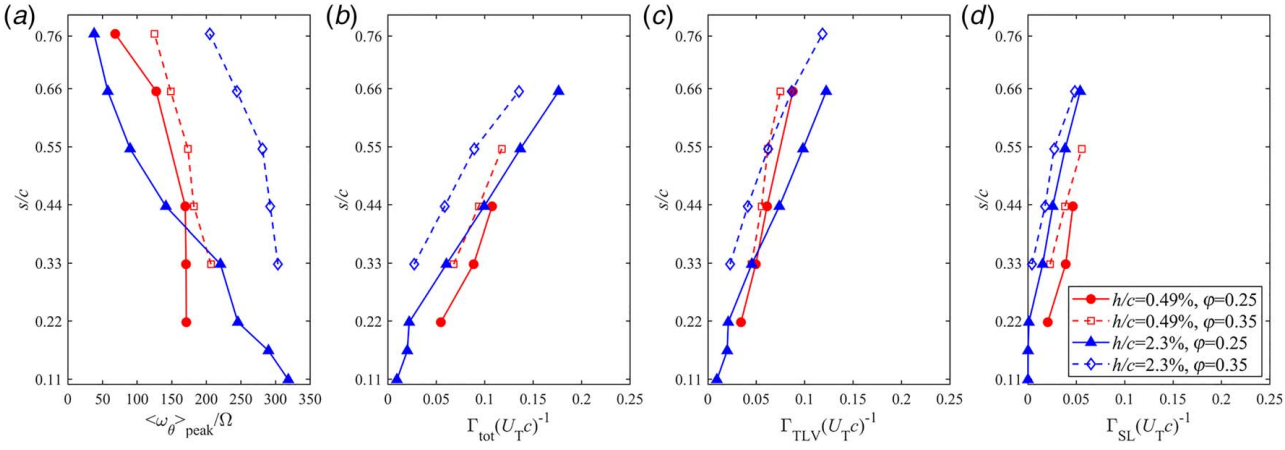

Fig. 10 (*a*) Magnitude of the peak circumferential vorticity within the TLV. (*b*, *c*) Circulation calculated by integrating the positive circumferential vorticity over: (*b*) the TLV and the shear layer, (*c*) the TLV only, and (*d*) the shear layer only.

increase with decreasing flowrate. However, the differences appear to be more prominent for Γ_{TLV} of the wide gap.

It would be of interest to determine how the location of initial TLV rollup affects differences in the distributions of Γ_{tot}. Hence, the same data are replotted in Fig. 11 versus s'/c, where s' is the chordwise distance from the point of initial rollup/detachment from the blade SS specified in Fig. 9(*a*) (e.g., $s'/c = s/c - 0.16$ for high flow rate and narrow gap). Surprisingly, the results for all four cases almost collapse, indicating that the rates of growth in Γ_{tot} after the TLV detaches from the blade are not substantially different. The (slightly) higher values for the narrow gap indicate a faster initial growth rate, upstream of the present range of measurements of this case, followed by a milder rate close to mid-chord. A series of other attempts to collapse the data further by including the effects of ψ_{SS} and φ with varying powers to non-dimensionalize Γ_{tot} have not led to further improvements in the collapse. However, interestingly, following classical theories for the blade circulation [3], when Γ_{tot} is scaled by $\psi_{ss}V_z l$, where l is the rotor blade pitch, Fig. 11(*b*) shows that for all the cases, the magnitude of $\Gamma_{tot}/(\psi_{ss}V_z l)$ at mid-chord is in the order of one. While such scaling does not improve the collapse of results, it does show that for the present data, *until mid-chord* $\Gamma_{tot}/(\psi_{ss}V_z l) \sim 2.2s'/c$. Lack of similar data prevents us from assessing whether this trend applies to other machines as well. Furthermore, we cannot extend this analysis to the aft part of the present blades since the sample areas do not cover that entire TLV once vortex breakdown occurs. In summary,

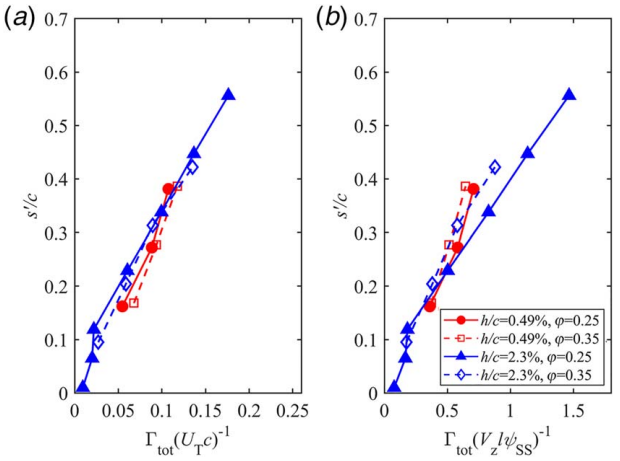

Fig. 11 Magnitude of the total circulation plotted versus the modified chordwise coordinate, s'/c: (*a*) scaled with $U_T c$ and (*b*) normalized by $\psi_{ss}V_z l$

Figs. 11(*a*) and 11(*b*) suggest that the primary effect of differences in blade loading among the present four cases is to shift the location of initial vortex rollup, and once it occurs, the growth rates of Γ_{tot} are quite similar.

The next analysis discussion is aimed at elucidating the mechanisms affecting the migration of the TLV away from the blade SS, which, as quantified below, is affected both by the leakage jet and flow induced by the image vortex on the other side of the endwall. Figure 12 summarizes the chordwise variations of the leakage flow, represented by averaging the axial and circumferential velocity components along a radial line extending from the SS corner of the blade tip to the endwall. Referring to Fig. 5(*b*), this line is located at $z/c_A = 0.256$ and extends from $r^* = 0.989$ to 1.0. Figures 12(*a*) and 12(*b*) show the distributions of axial ($U_{z,leak}$) and circumferential ($U_{\theta,leak}$) velocity components, respectively. Confined in the tip gaps, the gap-averaged radial velocity components are smaller than 10% of $U_{z,leak}$ or $U_{\theta,leak}$ and are not provided here. A scale on the top of Fig. 12(*b*) provides values for the circumferential leakage velocity in the rotor reference frame, $U^*_{\theta,leak}$. In subsequent discussions, * indicates data presented in the rotor reference frame. In all cases, the peak magnitudes of $U_{z,leak}$ are about 50% of the blade tip speed, but their chordwise distributions vary. For the narrow gap, at both flow rates, the magnitude of $U_{z,leak}$ in the mid-chord region decreases monotonically with increasing s/c, indicating that the blade is preferentially loaded further upstream. For the wide gap, $U_{z,leak}$ is either nearly zero or even positive near the leading edge, indicating weak blade loading, consistent with the delayed TLV rollup. The most notable flowrate effect in the distributions of $U_{\theta,leak}$ is the previously discussed region with $U_{\theta,leak} < 0$ at mid-chord at $\varphi = 0.35$, in contrast to the rapidly increasing $U_{\theta,leak} > 0$ at $\varphi = 0.25$. The latter is most likely affected by ingestion of the previous TLV remnants from the PS of the blade [36]. For the narrow gap, $U_{\theta,leak}$ also increases with decreasing flow rate, but it remains positive at $\varphi = 0.35$. The data are subsequently used for calculating the distributions of velocity component in a direction normal to the blade chord in the rotor reference frame ($U^*_{n,leak}$), which is shown in Fig. 12(*c*). Its trends can be used as an indirect indicator for variations in blade loading. The narrow gap results for both flow rates, which are available only for mid-chord, show similar decreasing trends with s/c, although the values for $\varphi = 0.35$ are slightly larger. With data available for a broader range for the wide gap, the flowrate effects are more evident. It appears that the two profiles have similar peak magnitude, but the curve for $\varphi = 0.25$ appear to be shifted to lower s/c relative to that for $\varphi = 0.35$. Hence, Fig. 12(*d*) shows the same data replotted versus s'/c. For the wide gap, for which the profiles cover the region even before TLV rollup, the two shifted profiles nearly collapse up to $s'/c \sim 0.2$. In fact, all the profiles nearly collapse around $s'/c = 0.2$, where $U^*_{n,leak}$ is more than 80% of the tip

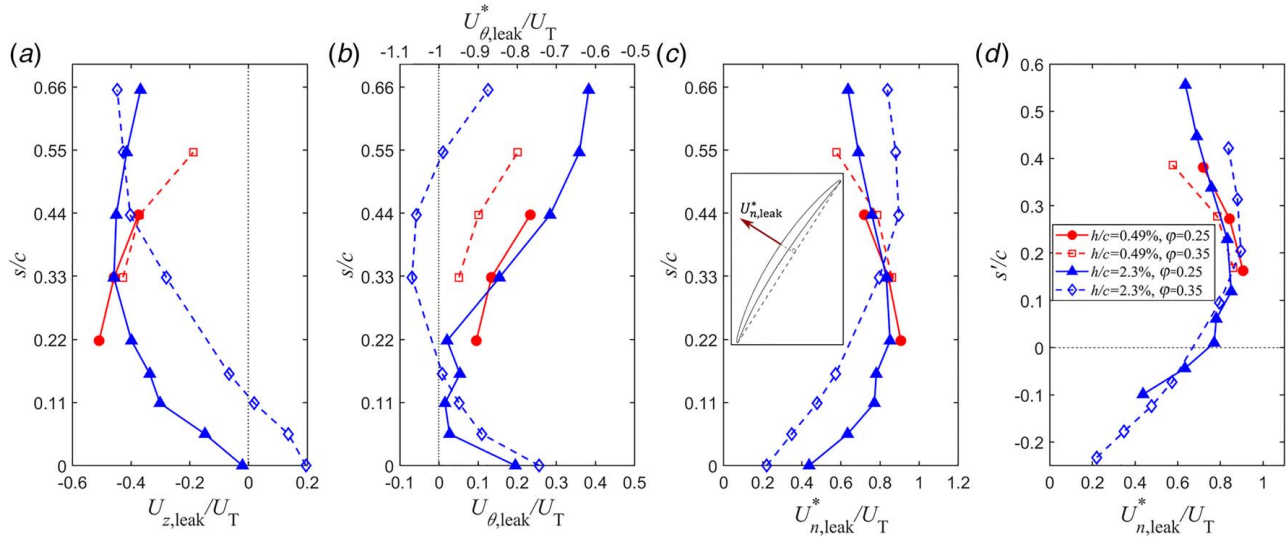

Fig. 12 The radially averaged distribution of leakage flow at the exit from the tip gap: (*a*) $U_{z,\mathrm{leak}}/U_\mathrm{T}$, (*b*) $U_{\theta,\mathrm{leak}}/U_\mathrm{T}$, with a second scale on top for $U^*_{\theta,\mathrm{leak}}/U_\mathrm{T}$, and (c) $U^*_{n,\mathrm{leak}}/U_\mathrm{T}$ with the inset showing its direction. (*d*) $U^*_{n,\mathrm{leak}}/U_\mathrm{T}$ plotted versus s'/c.

speed, but diverge and decrease in values at different rates further along the chord. Around the TLV detachment point ($s'=0$), $U^*_{n,\mathrm{leak}}/U_\mathrm{T}$ fall in the 0.7–0.8 range, which corresponds to about $\sqrt{\psi_{SS}}$ for both flow rates. While the evidence is limited to two cases, it appears that the TLV begins to detach when the leakage speed exceeds a threshold value, which for the present data is equal to $U_\mathrm{T}\sqrt{\psi_{SS}}$. Support for the existence of a critical detachment speed is provided by the cavitation images (Fig. 4) for all the cases. They show that the TLV detachment occurs in a region with a notable increase in the tip gap cavitation, indicating an increase in leakage velocity.

Discussion

This section focuses on trends and mechanisms associated with the TLV migration away from the blade SS. The distances from the TLV centers to the blade chord L_n as well as that from the blade SS L_n^{SS} are presented in Figs. 13(*a*) and 13(*b*), respectively, both as a function of s'/c. They are measured by projecting the vortex center, as well as the corresponding SS and chord locations onto the chord-normal direction (see inset in Fig. 13(*b*)). The difference between L_n and L_n^{SS}, i.e., the distance from the blade SS to the chord, varies along the chord with different trends before and after the mid-chord location. For all cases, L_n (Fig. 13(*a*)) grows with s'/c but with different slopes as well as initial values. The latter is initially larger for $\varphi=0.35$ for both gaps, consistent with the delayed rollup in regions where the blade is thicker. However, the low flow rate cases have higher growth rates of L_n versus s'. At $s'/c>0.2$, the values of L_n of the narrow gap are higher than those of the wide gap, reflecting the higher initial migration rate, as Figs. 7 and 8 demonstrate. Different trends emerge in the distributions of L_n^{SS} (Fig. 13(*b*)), which show that the TLV detachment from the blade SS is affected more strongly by the tip gap than the flow rate. In fact, for the wide gap, the two plots nearly collapse, and while rates vary for the narrow gap, the magnitudes are similar.

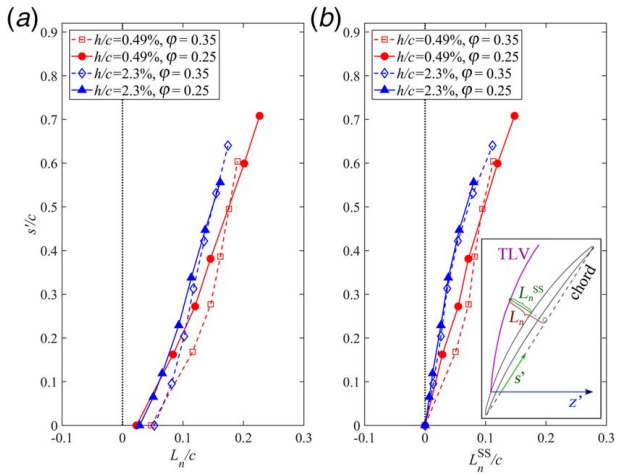

Fig. 13 The chord-normal distance from the TLV center to (*a*) the blade chord and (*b*) the blade SS tip corner plotted versus s'/c

Shifting the discussion to elucidation of the mechanism affecting the TLV migration rates, the values of L_n^{SS} are initially compared with a semi-empirical model introduced by Chen et al. [60]. Making an analogy to the time evolution of a two-dimensional vortex behind a bluff body, and combining it with empirical data from several sources, they conclude that $L_n^{SS}/z\left(\sqrt{\Delta P/\rho}/V_z\right)^{-1}=0.46$, where ΔP is the characteristic pressure difference across the blade, representing the blade loading. A different constant (0.19) has been subsequently measured by Kang and Hirsch [61], based on their cascade experiments. For present data, $\sqrt{\Delta P/\rho}$ is unavailable; hence, we have tried a series of surrogates, such as $U^*_{n,\mathrm{leak}}$ and $U^*_{\mathrm{leak}}=\sqrt{U^2_{z,\mathrm{leak}}+U^{*\,2}_{\theta,\mathrm{leak}}}$, and replaced z with z', the axial distance from the point of initial vortex rollup ($s'/c=0$), etc. The results (not shown) do not collapse irrespective of the variables used but vary from 0.1 to 0.4, i.e., they have the same order of magnitude as those reported in Refs. [60,61].

As an alternative approach, two likely mechanisms affect the TLV migration away from the blade SS. The first is the leakage flow jet that has a characteristic speed of $U^*_{n,\mathrm{leak}}$, which presumably acts on the vortex like a starting jet pushing a vortex ring [27,62–66]. The typical migration speed of a vortex ring during early phases of development is about 50% of the jet speed (e.g., Refs. [65,66]). Hence, one should expect that the initial rate of TLV detachment away from the blade should be close to $0.5U^*_{n,\mathrm{leak}}$. The second is the flow induced by the image vortex of the TLV on the other side of the endwall. Assuming a quasi-2D flow, this induced velocity can be calculated from

$$\vec{U}^*_{z,\mathrm{iv}}=\iint\frac{<\vec{\omega_\theta}>\times\vec{\lambda}}{2\pi\lambda^2}dA \tag{3}$$

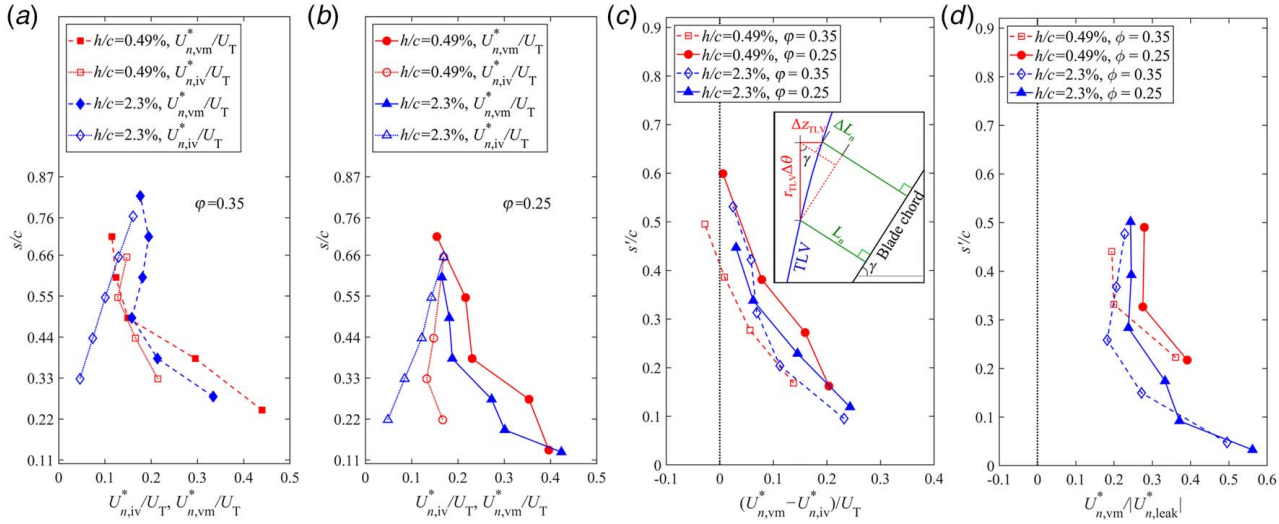

Fig. 14 The measured TLV migration rates away from the blade ($U^*_{n,vm}$, solid lines) are compared with the image vortex-induced velocity component normal to the blade chord ($U^*_{n,iv}$, dashed lines) for (*a*) $\varphi = 0.35$ and (*b*) $\varphi = 0.25$. (*c*) The values of $(U^*_{n,vm} - U^*_{n,iv})/U_T$ plotted versus s'/c. (*d*) The values of $U^*_{n,vm}/|U^*_{n,leak}|$ plotted versus s'/c.

where $\vec{\lambda}$ is a vector connecting an element within the TLV image to the TLV center and λ is its magnitude. The spatial integration is performed over the entire area of the image vortex using the same threshold vorticity discussed earlier. This analysis does not include the influence of the shear layer or its image since its effects almost cancel each other. The induced velocity component in a direction normal to the blade chord is then $U^*_{n,iv} = U^*_{z,iv} \sin\gamma$, where γ is the blade stagger angle. This velocity can be compared with the measured chord-normal migration rate, $U^*_{n,vm} = \Delta L_n/\Delta t$, where (see definitions in Fig. 14(*c*)) $\Delta L_n = r_{TLV}\Delta\theta\cos\gamma - \Delta z_{TLV}\sin\gamma$ is the displacement of TLV center between two measurement points, and Δt can be estimated using $\Delta t = r_{TLV}\Delta\theta/\overline{U^*_\theta}$. Here, $\Delta\theta$ is the angular difference between the two meridional planes involved, $\overline{U^*_\theta}$ is the circumferential velocity in the rotor reference frame spatially averaged over the vortex area and these two planes, and r_{TLV} is available in Fig. 9(*b*).

Comparisons between $U^*_{n,vm}$ and $U^*_{n,iv}$ for the two flow rates are provided separately in Figs. 14(*a*) and 14(*b*) to maintain clarity. Prior to mid-chord, the values of both $U^*_{n,vm}$ and $U^*_{n,iv}$ for the narrow gap are higher than those of the wide gap (Figs. 14(*a*) and 14(*b*)), in part due to differences in the TLV strength (Fig. 10(*c*)), but mostly due to the larger initial distance between TLV and its image (Fig. 11(*b*)) for the wide gap. In all cases, $U^*_{n,vm} > U^*_{n,iv}$ at low *s*/*c*, but the differences between them diminish deeper in the passage. This trend is further demonstrated in Fig. 14(*c*) by showing the values of $(U^*_{n,vm} - U^*_{n,iv})/U_T$ plotted versus s'/c. Although they do not collapse, they all display similar trends, decreasing from ~0.25 to zero with increasing s'/c. This observation suggests that when the TLV is located near the SS, other contributors, such as the tip leakage jet, might play significant roles in the TLV detachment, but the image vortex becomes the main driver at mid-chord as the influence of the jet diminishes. Similar phenomena occur, e.g., for vortex rings, where the self-induced motion of the vortex becomes the main driver as the distance from the origin of the ring increases [62–64]. The corresponding values of $U^*_{n,vm}/|U^*_{n,leak}|$ shown in Fig. 14(*d*) indicate that for the wide gap, where $U^*_{n,vm}$ is available near the TLV detachment point, the initial values for both flow rates are nearly 0.5. For the narrow gap, where the available data are limited to planes where the TLV is already detached from the SS (Figs. 7 and 8), the results also tend toward what appears to be similar initial values. These trends are consistent with our postulate that the leakage jet is the primary driver for TLV detachment during early phases. Further along the blade, as the values of $U^*_{n,vm}$ decrease, but do not diminish, the image vortex becomes the driver. In summary, Fig. 14(*d*) suggests that the early migration rate of the TLV is about 50% of the leakage jet, and Fig. 14(*c*) demonstrates that deeper in the passage, the migration rate is nearly equal to the flow induced by the image vortex.

Conclusions

High-speed cavitation imaging and SPIV measurements examine the effects of tip gap sizes and operating conditions on the flow structure in the tip region of an axial turbomachine. Data obtained for two very different tip gaps (0.49% and 2.3% of the blade chord length) and at flow rates include the machine performance, evolution of leakage velocity, as well as the TLV structure, strength, and trajectory in the passage. Consistent with prior studies (e.g., Ref. [17]), increasing the tip clearance causes substantial degradation of the machine performance. Hence, the distributions of leakage velocity as well as the TLV strength, location of initial rollup, growth rate, and migration in the passage are also altered. Common features include the following: (i) The TLV is a three-dimensional swirling jet with significant vorticity components in all three directions, but the circumferential component is dominant. (ii) For all cases and locations in the passage, a region with elevated positive circumferential velocity (in the same direction as the blade rotation) develops radially inward from the TLV center. (iii) In the aft part of the passage, vortex breakdown causes rapid growth of the area covered by the TLV and a reduction in the peak vorticity magnitude. Enlarging the tip clearance delays the vortex breakup at high flow rates, but causes earlier breakup under pre-stall conditions, presumably due to the propagation of more prevalent backflow vortices [38] across the wider gap. (iv) The endwall boundary layer separates at the point where the backward leakage flow meets the passage flow, forming a layer with counter-rotating vorticity. For the narrow gap, this layer is entrained radially inward by the TLV and creates a ring that surrounds the entire vortex. Conversely, for the wide gap, the layer remains largely above the TLV.

Detachment of the TLV from the blade SS occurs when the chord-normal component of the tip leakage velocity exceeds a threshold level of 70%–80% of the blade tip speed. Reducing the flow rate or decreasing the tip gap shifts the detachment point and location of peak leakage velocity upstream. When the total circulation fed into the blade SS is plotted versus the chordwise distance from the TLV detachment point, results for the two gaps and flow rates nearly collapse. The magnitude of this circulation at mid-chord

is consistent with classical theories, i.e., nearly equal to $\psi_{ss}V_z l$. Furthermore, the distributions of leakage velocity plotted versus distance from the TLV detachment point collapse until mid-chord and then diverge. These findings imply that the primary gap or flowrate effect on the shed circulation and leakage velocity is to shift the TLV detachment point.

Once it detaches, the rate at which the TLV migrates away from the blade SS decreases with increasing gap size but does not differ significantly with flowrate for the same gap. Consequently, the length of and circulation in the shear layer connecting the TLV to the SS tip corner increase with decreasing gap, and accordingly, the growth rate of the TLV circulation decreases. For all cases, two mechanisms affect the TLV migration rate away from the blade. In early phases, the leakage jet pushes the TLV away from the blade; hence, the initial migration speed is about 50% of the leakage velocity, similar to starting vortex rings. With increasing distance from the SS, the effect of the leakage jet diminishes, and the TLV migration rate approaches the velocity induced by the image vortex on the other side of the endwall. Consequently, the TLV migration increases with decreasing tip gap, i.e., the distance between the TLV and its image, as well as the increasing initial TLV strength with decreasing flow rate and gap size. The implication of these observations is that the performance degradation occurring as the tip gap is widened is *not* associated with an increase in the area influenced directly by the TLV, presumably, the TLV-induced blockage. Conversely, increasing the tip gap keeps the TLV closer to the blade SS and delays the TLV breakdown at high flow rates. Furthermore, by the mid chord, the gap-related differences in the radial location of the TLV center are only about 2% of the blade span.

Acknowledgment

This project is funded in part by NASA Glenn Research Center under grant number NNX11AI21A (Funder ID: 10.13039/100006193) and in part by ONR under grant number N00014-09-1-0353 (Funder ID: 10.13039/100000006). The authors would like to thank Chunill Hah and Michael Hathaway from NASA/Glenn for their guidance and for modifying the LSAC blade geometries to satisfy the constraints of the JHU index-matched facility. We would also like to thank Yury Ronzhes for designing all the mechanical components of this facility.

Nomenclature

c = rotor blade tip chord
h = width of the rotor blade tip gap
s = rotor blade chordwise coordinate
t = time
L = distance from the hub surface to the inner casing endwall
P = static pressure
c_A = rotor blade axial tip chord
s_{det} = chordwise coordinate of the TLV detachment point from the blade SS
z_{sep} = axial coordinate for the point of endwall boundary layer separation
L_n = distance from the TLV center to the blade chord in the chord-normal direction
U_T = rotor blade tip speed
V_z = mean incoming flow velocity
r^* = non-dimensional radial coordinate
r^*_{TLV} = non-dimensional radial coordinate of the TLV center
$U^*_{n,iv}$ = induced velocity component normal to the blade chord by the "image" vortex
$U^*_{z,iv}$ = induced velocity by the "image" vortex
$U^*_{n,vm}$ = measured vortex migration rate from the blade suction side in a direction normal to the blade chord in the rotor reference frame
L_n^{SS} = distance from the TLV center to the blade SS in the chord-normal direction
r, z, θ = radial, axial and circumferential coordinates
z_{TLV}, r_{TLV} = axial and radial coordinates of the TLV center
U_r, U_z, U_θ = ensemble-averaged radial, axial and circumferential velocity
$U_{z,leak}, U_{\theta,leak}$ = axial and circumferential components of the radially averaged mean leakage velocity at the exit of the blade tip reference frame
γ = rotor blade stagger angle
λ = distance between the TLV center and "image" vorticity element
ρ = density
Γ_{TLV} = circulation in the TLV only
Γ_{SL} = circulation in the shear layer only
φ = flow coefficient
ψ_{SS} = static-to-static pressure coefficient
$\omega_r, \omega_z, \omega_\theta$ = radial, axial, circumferential vorticity
Ω = rotor angular velocity
Γ_{tot} = total circulation in the TLV and shear layer
$\langle\ \rangle$ = ensemble average

Superscript

$*$ = indicate variables in the rotor reference frame
SS = suction side

Subscript

A = axial
iv = image vortex (induced motion)
leak = tip leakage (velocity)
n = normal (to the blade chord)
SL = shear layer
SS = static-to-static (pressure)
TLV = tip leakage vortex
tot = total
vm = (measured) vortex migration

References

[1] Pampreen, R. C., 1993, *Compressor Surge and Stall*, Concepts ETI, Norwich, VT.
[2] Cumpsty, N. A., 2004, *Compressor Aerodynamics*, 2nd ed., Krieger Pub, Melbourne, FL.
[3] Lakshminarayana, B., 1996, *Fluid Dynamics and Heat Transfer of Turbomachinery*, John Wiley & Sons, New York, NY.
[4] Khalid, S. A., Khalsa, A. S., Waitz, I. A., Tan, C. S., Greitzer, E. M., Cumpsty, N. A., Adamczyk, J. J., and Marble, F. E., 1999, "Endwall Blockage in Axial Compressors," ASME J. Turbomach., **121**(3), pp. 499–509.
[5] Ciorciari, R., Lesser, A., Blaim, F., and Niehuis, R., 2012, "Numerical Investigation of Tip Clearance Effects in an Axial Transonic Compressor," J. Therm. Sci., **21**(2), pp. 109–119.
[6] Gourdain, N., Wlassow, F., and Ottavy, X., 2012, "Effect of Tip Clearance Dimensions and Control of Unsteady Flows in a Multi-Stage High-Pressure Compressor," ASME J. Turbomach., **134**(5), p. 051005.
[7] You, D., Wang, M., Moin, P., and Mittal, R., 2006, "Effects of Tip-Gap Size on the Tip-Leakage Flow in a Turbomachinery Cascade," Phys. Fluids, **18**(10), pp. 1–14.
[8] Hah, C., Hathaway, M., and Katz, J., 2014, "Investigation of Unsteady Flow Field in a Low-Speed One and a Half Stage Axial Compressor: Effects of Tip Gap Size on the Tip Clearance Flow Structure At Near Stall Operation," ASME Turbo Expo, Düsseldorf, Germany, June 16–204, Paper No. GT2014-27094, p. V02DT44A040.
[9] Hah, C., Hathaway, M., Katz, J., and Tan, D., 2015, "Investigation of Unsteady Tip Clearance Flow in a Low-Speed One and Half Stage Axial Compressor With LES and PIV," ASME/JSME/KSME 2015 Joint Fluids Engineering Conference Volume 1: Symposia, Seoul, South Korea, July 26–31, Paper No. AJK2015-02061, p. V001T02A002.
[10] Storer, J., and Cumpsty, N., 1991, "Tip Leakage Flow in Axial Compressors," ASME J. Turbomach., **113**(2), pp. 252–259.
[11] Muthanna, C., and Devenport, W. J., 2004, "Wake of a Compressor Cascade With Tip Gap. Part 1: Mean Flow and Turbulence Structure," AIAA J., **42**(11), pp. 2320–2331.
[12] Wang, Y., and Devenport, W. J., 2004, "Wake of a Compressor Cascade With Tip Gap, Part 2: Effects of Endwall Motion," AIAA J., **42**(11), pp. 2332–2340.
[13] Ma, R., and Devenport, W. J., 2007, "Tip Gap Effects on the Unsteady Behavior of a Tip Leakage Vortex," AIAA J., **45**(7), pp. 1713–1724.

[14] Williams, R., Gregory-Smith, D., He, L., and Ingram, G., 2010, "Experiments and Computations on Large Tip Clearance Effects in a Linear Cascade," ASME J. Turbomach., **132**(4), p. 021018.
[15] Inoue, M., Kuroumaru, M., and Fukuhara, M., 1986, "Behavior of Tip Leakage Flow Behind an Axial Compressor Rotor," ASME J. Eng. Gas Turbines Power, **108**(1), pp. 7–14.
[16] Inoue, M., and Kuroumaru, M., 1989, "Structure of Tip Clearance Flow in an Isolated Axial Compressor Rotor," ASME J. Turbomach., **111**(3), p. 250.
[17] Goto, A., 1992, "Three-Dimensional Flow and Mixing in an Axial Flow Compressor With Different Rotor Tip Clearances," ASME J. Turbomach., **114**(3), pp. 675–685.
[18] Doukelis, A., Mathioudakis, K., and Papailiou, K., 1998, "The Effect of Tip Clearance Gap Size and Wall Rotation on the Performance of a High Speed-Annular Compressor Cascade," International Gas Turbine and Aeroengine Congress and Exposition, Stockholm, Sweden, June 2–5, Paper No. 98-GT-38, p. V001T01A011.
[19] Peacock, R. E., 1983, "A Review of Turbomachinery Tip Gap Effects Part 1: Cascades," Int. J. Heat Fluid Flow, **3**(4), pp. 185–193.
[20] Peacock, R. E., 1983, "A Review of Turbomachinery Tip Gap Effects Part 2: Rotating Machinery," Int. J. Heat Fluid Flow, **4**(1), pp. 3–16.
[21] Sakulkaew, S., Tan, C. S., Donahoo, E., Cornelius, C., and Montgomery, M., 2013, "Compressor Efficiency Variation With Rotor Tip Gap From Vanishing to Large Clearance," ASME J. Turbomach., **135**(3), p. 031030.
[22] März, J., Hah, C., and Neise, W., 2002, "An Experimental and Numerical Investigation Into the Mechanisms of Rotating Instability," ASME J. Turbomach., **124**(7), pp. 367–375.
[23] Liu, B., Wang, H., Liu, H., Yu, H., Jiang, H., and Chen, M., 2004, "Experimental Investigation of Unsteady Flow Field in the Tip Region of an Axial Compressor Rotor Passage at Near Stall Condition With SPIV," ASME J. Turbomach., **126**(3), pp. 360–374.
[24] Yu, X. J., and Liu, B. J., 2007, "Stereoscopic PIV Measurement of Unsteady Flows in an Axial Compressor Stage," Exp. Therm. Fluid Sci., **31**(8), pp. 1049–1060.
[25] Zhang, Z., Yu, X., and Liu, B., 2012, "Characteristics of the Tip Leakage Vortex in a Low-Speed Axial Compressor With Different Rotor Tip Gaps," ASME Turbo Expo 2012, Copenhagen, Denmark, June 11–15, Paper No. GT2012-69148, pp. 311–322.
[26] Miorini, R. L., Wu, H., and Katz, J., 2012, "The Internal Structure of the Tip Leakage Vortex Within the Rotor of an Axial Waterjet Pump," ASME J. Turbomach., **134**(3), p. 031018.
[27] Wu, H., Miorini, R. L., and Katz, J., 2011, "Measurements of the Tip Leakage Vortex Structures and Turbulence in the Meridional Plane of an Axial Water-Jet Pump," Exp. Fluids, **50**(4), pp. 989–1003.
[28] Wu, H., Miorini, R. L., Tan, D., and Katz, J., 2012, "Turbulence Within the Tip-Leakage Vortex of an Axial Waterjet Pump," AIAA J., **50**(11), pp. 2574–2587.
[29] Wu, H., Tan, D., Miorini, R. L., and Katz, J., 2011, "Three-Dimensional Flow Structures and Associated Turbulence in the Tip Region of a Waterjet Pump Rotor Blade," Exp. Fluids, **51**(6), pp. 1721–1737.
[30] Uzol, O., Chow, Y. C., Katz, J., and Meneveau, C., 2002, "Unobstructed PIV Measurements Within an Axial Turbo-Pump Using Liquid and Blades With Matched Refractive Indices," Exp. Fluids, **33**(6), pp. 909–919.
[31] Soranna, F., Chow, Y.-C., Uzol, O., and Katz, J., 2006, "The Effect of Inlet Guide Vanes Wake Impingement on the Flow Structure and Turbulence Around a Rotor Blade," ASME J. Turbomach., **128**(1), p. 82.
[32] Soranna, F., Chow, Y.-C., Uzol, O., and Katz, J., 2008, "Turbulence Within a Turbomachine Rotor Wake Subject to Nonuniform Contraction," AIAA J., **46**(11), pp. 2687–2702.
[33] Wasserbauer, C. A., Weaver, H. F., and Senyitko, R. G., 1995, *NASA Low-Speed Axial Compressor for Fundamental Research*, NASA Lewis Research Center, Cleveland, OH.
[34] Wisler, D. C., 1977, *Core Compressor Exit Stage Study: Volume I—Blade Design*, General Electric Co.; Aircraft Engine Group., Cincinnati, OH.
[35] Tan, D., Li, Y., Wilkes, I., Miorini, R. L., and Katz, J., 2014, "PIV Measurements of the Flow in the Tip Region of a Compressor Rotor," ASME 2014 4th Joint US-European Fluids Engineering Division Summer Meeting Collocated With the ASME 2014 12th International Conference on Nanochannels, Microchannels, and Minichannels. Volume 1B, Symposia, Chicago, IL, Aug. 3–7, Paper No. FEDSM2014-21593, p. V01BT10A031.
[36] Tan, D., Li, Y., Wilkes, I., Miorini, R. L., and Katz, J., 2015, "Visualization and Time-Resolved Particle Image Velocimetry Measurements of the Flow in the Tip Region of a Subsonic Compressor Rotor," ASME J. Turbomach., **137**(4), p. 041007.
[37] Tan, D., Li, Y., Chen, H., Wilkes, I., and Katz, J., 2015, "The Three Dimensional Flow Structure and Turbulence in the Tip Region of an Axial Flow Compressor," ASME Turbo Expo 2015: Turbine Technical Conference and Exposition, Montreal, QC, Canada, June 15–19, Paper No. GT2015-43385, p. V02AT37A036.
[38] Chen, H., Li, Y., Tan, D., and Katz, J., 2017, "Visualizations of Flow Structures in the Rotor Passage of an Axial Compressor at the Onset of Stall," ASME J. Turbomach., **139**(4), p. 041008.
[39] Furukawa, M., Inoue, M., Saiki, K., and Yamada, K., 1999, "The Role of Tip Leakage Vortex Breakdown in Compressor Rotor Aerodynamics," ASME J. Turbomach., **121**(3), pp. 469–480.
[40] Schlechtriem, S., and Lotzerich, M., 1997, "Breakdown of Tip Leakage Vortices in Compressors at Flow Conditions Close to Stall," International Gas Turbine and Aeroengine Congress and Exposition, Orlando, FL, June 2–5, Paper No. 97-GT-41, pp. 1–8.
[41] Yamada, K., Funazaki, K., and Furukawa, M., 2007, "The Behavior of Tip Clearance Flow at Near-Stall Condition in a Transonic Axial Compressor Rotor," ASME Turbo Expo 2007, Montreal, QC, Canada, May 25–17, Paper No. GT2007-27725, pp. 295–306.
[42] Li, Y., Tan, D., Chen, H., and Katz, J., 2015, "Effects of Tip Gap Size on the Flow Structure in the Tip Region of an Axial Turbomachine," ASME/JSME/KSME 2015 Joint Fluids Engineering Conference Volume 1: Symposia, Seoul, South Korea, July 26–31, Paper No. AJK2015-33787, p. V001T33A023.
[43] Li, Y., Chen, H., Tan, D., and Katz, J., 2016, "Effects of Tip Clearance and Operating Conditions on the Flow Structure and Reynolds Stresses Within an Axial Compressor Rotor Passage," ASME Turbo Expo, Seoul, South Korea, June 13–17, Paper No. GT2016-57050, p. V02AT37A030.
[44] Bai, K., and Katz, J., 2014, "On the Refractive Index of Sodium Iodide Solutions for Index Matching in PIV," Exp. Fluids, **55**(4), pp. 1–6.
[45] Wieneke, B., 2005, "Stereo-PIV Using Self-Calibration on Particle Images," Exp. Fluids, **39**(2), pp. 267–280.
[46] Roth, G. I., and Katz, J., 2001, "Five Techniques for Increasing the Speed and Accuracy of PIV Interrogation," Meas. Sci. Technol., **12**(3), pp. 238–245.
[47] Sridhar, G., and Katz, J., 1995, "Drag and Lift Forces on Microscopic Bubbles Entrained by a Vortex," Phys. Fluids, **7**(2), pp. 389–399.
[48] Tan, D., Li, Y., Wilkes, I., Vagnoni, E., Miorini, R., and Katz, J., 2015, "Experimental Investigation of the Role of Large Scale Cavitating Vortical Structures in Performance Breakdown of an Axial Waterjet Pump," ASME J. Fluids Eng., **137**(11), p. 111301.
[49] Chen, H., Doeller, N., Li, Y., and Katz, J., 2017, "Measurements of the Flow and Pressure Within an Axial Waterjet Pump During Cavitation Breakdown," International Symposium on Transporat Phenomena and Dynamics of Rotating Machinery, Maui, HI, Dec. 16–21, pp. 1–12.
[50] Lindau, J. W., Pena, C., Baker, W. J., Dreyer, J. J., Moody, W. L., Kunz, R. F., and Paterson, E. G., 2012, "Modeling of Cavitating Flow Through Waterjet Propulsors," Int. J. Rotating Mach., **2012**, pp. 1–13.
[51] Farrell, K. J., and Billet, M. L., 1994, "A Correlation of Leakage Vortex Cavitation in Axial-Flow Pumps," ASME J. Fluids Eng., **116**(3), pp. 551–557.
[52] Yamamoto, K., and Tsujimoto, Y., 2009, "Backflow Vortex Cavitation and Its Effects on Cavitation Instabilities," Int. J. Fluid Mach. Syst., **2**(1), pp. 40–54.
[53] Yamanishi, N., Fukao, S., Qiao, X., Kato, C., and Tsujimoto, Y., 2007, "LES Simulation of Backflow Vortex Structure at the Inlet of an Inducer," ASME J. Fluids Eng., **129**(5), pp. 587–594.
[54] Yokota, K., Mitsuda, K., Tsujimoto, Y., and Kato, C., 2004, "A Study of Vortex Structure in the Shear Layer Between Main Flow and Swirling Backflow," JSME Int. J., Ser. B, **47**(3), pp. 541–548.
[55] Yokota, K., Kurahara, K., Kataoka, D., Tsujimoto, Y., and Acosta, A. J., 1999, "A Study of Swirling Backflow and Vortex Structure at the Inlet of an Inducer," JSME Int. J., **42**(3), pp. 451–459.
[56] Day, I. J., 2015, "Stall, Surge, and 75 Years of Research," ASME J. Turbomach., **138**(1), p. 011001.
[57] Pullan, G., Young, A. M., Day, I. J., Greitzer, E. M., and Spakovszky, Z. S., 2015, "Origins and Structure of Spike-Type Rotating Stall," ASME J. Turbomach., **137**(5), p. 051007.
[58] Day, I. J., 1993, "Stall Inception in Axial Flow Compressors," ASME J. Turbomach., **115**(1), pp. 1–9.
[59] You, D., Wang, M., Moin, P., and Mittal, R., 2007, "Large-Eddy Simulation Analysis of Mechanisms for Viscous Losses in a Turbomachinery Tip-Clearance Flow," J. Fluid Mech., **586**(Sept.), pp. 177–204.
[60] Chen, G. T., Greitzer, E. M., Tan, C. S., and Marble, F. E., 1991, "Similarity Analysis of Compressor Tip Clearance Flow Structure," ASME J. Turbomach., **113**(2), p. 260.
[61] Kang, S., and Hirsch, C., 1993, "Experimental Study on the Three- Dimensional Flow Within a Compressor Cascade With Tip Clearance : Part I—Velocity and Pressure Fields," ASME J. Turbomach., **115**(3), pp. 435–443.
[62] Gharib, M., Rambod, E., and Shariff, K., 1998, "A Universal Time Scale for Vortex Ring Formation," J. Fluid Mech., **360**(Apr.), pp. 121–140.
[63] Rosenfeld, M., Rambod, E., and Gharib, M., 1998, "Circulation and Formation Number of Laminar Vortex Rings," J. Fluid Mech., **376**(Dec.), pp. 297–318.
[64] Shusser, M., and Gharib, M., 2000, "Energy and Velocity of a Forming Vortex Ring," Phys. Fluids, **12**(3), pp. 618–621.
[65] Mohseni, K., and Gharib, M., 1998, "A Model for Universal Time Scale of Vortex Ring Formation," Phys. Fluids, **10**(10), pp. 2436–2438.
[66] Mohseni, K., 2006, "A Formulation for Calculating the Translational Velocity of a Vortex Ring or Pair," Bioinspiration Biomimetics, **1**(4), pp. S57–S64.